PCCP

Physical Chemistry Chemical Physics

rsc.li/pccp

ROYAL SOCIETY
OF **CHEMISTRY**
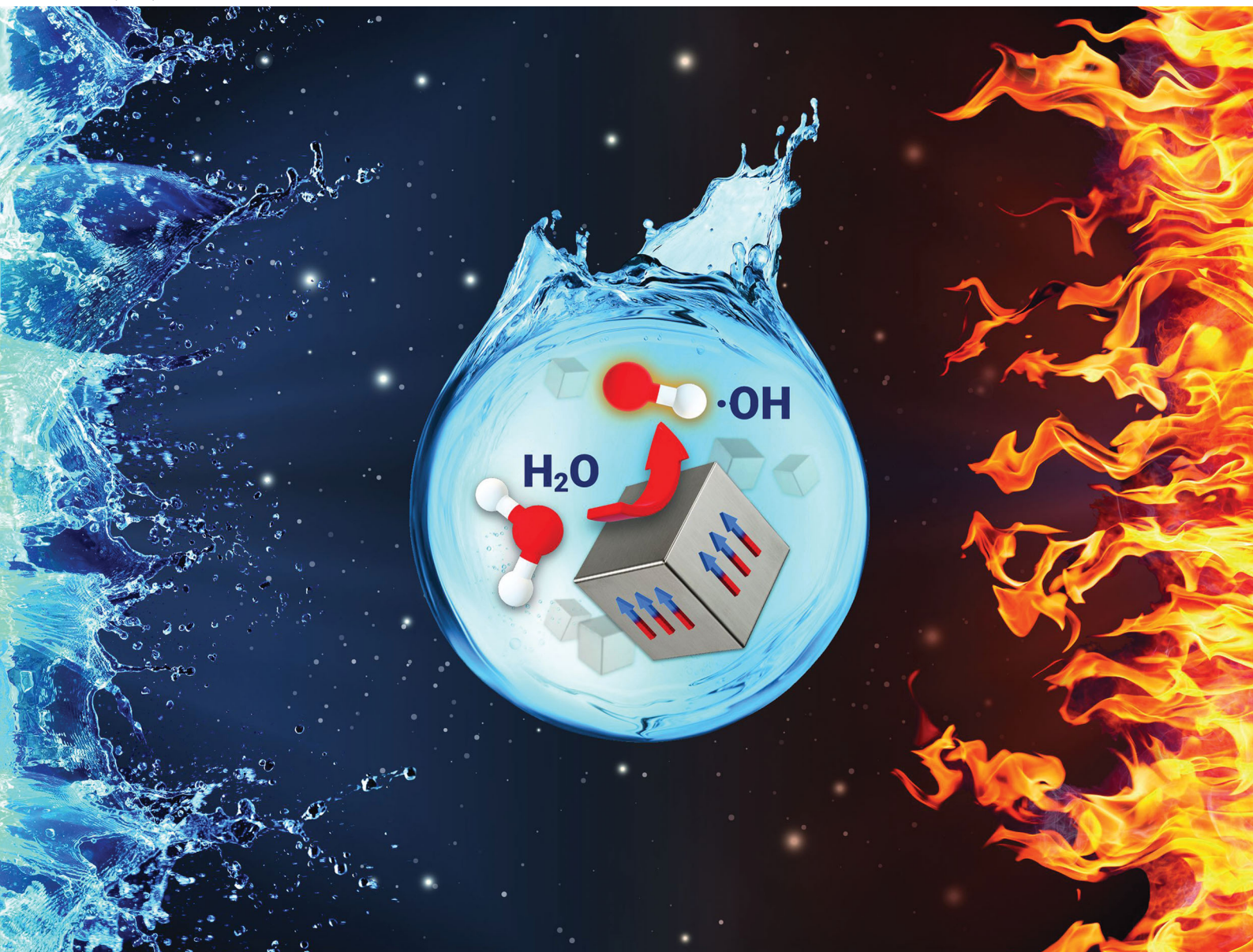
PAPER
Patrick Braeutigam *et al.*
Pyrocatalytic oxidation – strong size-dependent
poling effect on catalytic activity of pyroelectric
BaTiO$_3$ nano- and microparticles

Check for updates

Pyrocatalytic oxidation – strong size-dependent poling effect on catalytic activity of pyroelectric BaTiO₃ nano- and microparticles†

Sascha Raufeisen, [ab] Peter Neumeister,[c] Johannes R. Buchheim,[ab] Michael Stelter[abd] and Patrick Braeutigam ⭐[ab]

Pyrocatalysis is an emerging advanced oxidation process for wastewater remediation with the potential for thermal energy harvesting and utilization. Although several studies explored the potential of new pyrocatalyst materials to degrade harmful organic water pollutants, the role of important material properties and electric poling procedures on the pyrocatalytic activity is still unclear. In this work, we investigate the interdependence between particle size, electric poling and pyrocatalytic activity of BaTiO₃ powders with nominal particle sizes of 100, 200 and 500 nm by using the dichlorofluorescein redox assay. Depending on the particle size, the influence of surface area or phase composition on the pyrocatalytic activity predominates. Moreover, we demonstrate that poling of pyrocatalysts leads to a strong size-dependent increase of pyrocatalytic activity. This poling effect increases with particle size up to +247% and can be explained with size-dependent changes in phase composition and domain structure. Combining all results, the progression of the pyrocatalytic activity as a function of particle size was derived and a future strategy for maximizing the catalytic performance of pyrocatalysts was developed. This study greatly improves the understanding about the role of important material properties and electric poling on pyrocatalytic activity, thus enabling an effective catalyst design. With the help of highly active catalysts, the pyrocatalytic process can take the next step in its development into a new and energy-efficient advanced oxidation process for water remediation.

1 Introduction

Ongoing progress in medical research in combination with an ageing society led to the widespread release of a large number of pharmaceuticals into the water cycle.[1,2] Enabled by advancements in analytical techniques, trace amounts of these pharmaceuticals as well as their metabolites and transformation products were detected in almost any fresh water resource.[3–5] Since urban wastewater treatment plants are the main emission source of such potentially toxic and ecotoxic micropollutants, the introduction of advanced oxidation processes (AOPs) is discussed as part of an additional water treatment stage.[6–8]

The purpose of AOPs is the oxidative degradation of (micro)-pollutants to nontoxic transformation products with the help of *in situ* generated free radical species like hydroxyl radicals •OH.[9,10] Well-established AOP techniques are ozonation (O₃), Fenton (Fe^{2+}/H_2O_2), sonolysis, UV oxidation, electrocatalysis and photocatalysis (*e.g.* UV/TiO₂).[11–16] Photocatalytic techniques in particular were greatly improved over the last years due to the development of innovative materials and material combinations.[17] One driving force for material innovations is the reduction of energy demand and costs for the photoexcitation. This reduction can be achieved by adjusting the absorption of the photocatalyst toward the solar spectrum, thus enabling the harvesting of solar energy.[18,19]

The harvesting of energy from the environment and its conversion into chemical energy for wastewater remediation can also be reached with an emerging AOP technique, the pyrocatalysis.[20] This technique utilizes the pyroelectric effect of crystals with a spontaneous polarization, which changes in response to temperature fluctuations. Under thermal cycling,

[a] *Institute of Technical Chemistry and Environmental Chemistry, Friedrich Schiller University Jena, Philosophenweg 7a, 07743 Jena, Germany. E-mail: patrick.braeutigam@uni-jena.de*

[b] *Center for Energy and Environmental Chemistry (CEEC Jena), Friedrich Schiller University Jena, Philosophenweg 7a, 07743 Jena, Germany*

[c] *Fraunhofer IKTS, Fraunhofer Institute for Ceramic Technologies and Systems, Winterbergstraße 28, 01277 Dresden, Germany*

[d] *Fraunhofer IKTS, Fraunhofer Institute for Ceramic Technologies and Systems, Michael-Faraday-Straße 1, 07629 Hermsdorf, Germany*

† Electronic supplementary information (ESI) available: Contains reaction scheme of DCF assay, DCF calibration data, sample allocation during experiment, detailed temperature profiles, X-ray diffractograms and results for Rietveld refinements for BT samples, and BET specific surface area for BT samples. See DOI: 10.1039/d0cp03158e

23464 | *Phys. Chem. Chem. Phys.*, 2020, **22**, 23464–23473

This journal is © the Owner Societies 2020

transient variations of the polarization magnitude occur and lead to a build-up of polarization charges on the pyroelectric crystal surface. Although these polarization charges are screened by compensation charges at equilibrium, transient net charges can trigger redox reactions. Thus, pyroelectrically generated reactive oxygen species (ROS) such as ·OH can convert organic micropollutants into nontoxic degradation products.

The application of pyrocatalysis for wastewater remediation has the potential for a great reduction of energy demand and costs by harvesting thermal energy from natural temperature gradients as well as waste heat from industrial processes.[21] However, there is a great gap in knowledge about the exact catalytic mechanism as well as the influence of essential process/reaction/material parameters on the pyrocatalytic activity. In recent years, various experimental and some theoretical studies investigated the catalytic potential of pyroelectric materials for water remediation (disinfection,[20] micropollutant degradation[22,23]) but also for hydrogen generation through water splitting.[24–26] Several studies introduced new pyrocatalysts ($LiNbO_3$, $LiTaO_3$, $BaTiO_3$, $BiFeO_3$, *etc.*) with different particle shapes (*e.g.* nanoparticles, nanofibers) and explored their potential to degrade model substances like rhodamine B.[27,28] In addition, Zhang *et al.* developed a number of concepts to increase the activity of pyrocatalysts such as the combination with co-catalysts or cycling the temperature around the Curie temperature T_C of materials with low T_C (high pyroelectric coefficient).[28]

The experimental studies were important in order to show that the concept of a pyrocatalytic process can be transferred to a variety of different pyroelectric materials and applications. Unfortunately, they are not comparable and therefore not suited for a detailed investigation of the influence of important material parameters such as the particle size/shape, the pyroelectric coefficient or the relative permittivity on the pyrocatalytic activity. Three main reasons for this are (i) the broad variety of process parameters, especially the temperature curves used for thermal excitation, (ii) the lack of information about important material properties such as crystallographic structure, particle size/shape distribution as well as specific surface area, and (iii) the comparison of materials from different synthesis routes.[29] Only studies that allow a direct comparison of pyroelectric catalyst materials with identical process/reaction parameters in combination with an adequate material characterization are suited for a maximization of catalytic activity. Furthermore, the potential benefits of an electric poling procedure on the catalytic activity of pyrocatalysts were ignored with few exceptions.[23,30,31] This is remarkable, since several studies of the related piezocatalysis have shown a strong increase of piezocatalytic activity through such a remanent alignment of ferroelectric dipoles inside ferroelectric particles.[32–34]

In this work, the influence of the particle size on the pyrocatalytic activity of $BaTiO_3$ powder (BT) catalysts containing nanoparticles with nominal particle sizes of 100, 200 and 500 nm was investigated. It was shown under directly comparable conditions that the pyrocatalytic activity of BT catalysts correlates mainly with their BET surface area. However, a comparison with literature data led to the overall picture that the importance of size-dependent phase composition and tetragonality increases strongly for smaller particles. Moreover, the catalytic activity of BT catalysts was greatly increased through poling up to +247%. It was shown under directly comparable conditions that the relative pyrocatalytic activity enhancement by poling is size-dependent and increases with particle size. This finding was explained with the increased fraction of tetragonal phase, the transition from ferroelectric single-domain to multidomain crystals, as well as the better movability of domain walls of larger particles. These size-dependent aspects led to an improved alignment of randomly distributed ferroelectric dipoles in larger, multidomain particles during poling, which in turn led to a higher relative increase of pyrocatalytic activity. All results were compared with literature data and a future strategy for maximizing the catalytic performance of pyrocatalysts was developed. With the help of this strategy, the pyrocatalytic process can take the next step in its development into a new AOP technique for water remediation, accompanied with a great potential for thermal energy harvesting.

2 Experimental

2.1 Reagents and chemicals

$BaTiO_3$ powders with different nominal particle sizes in the range from 100 to 500 nm were supplied by US Research Nanomaterials, Inc. (BT100: 100 nm; BT200: 200 nm, BT500: 500 nm; all 99.9%). 2′,7′-Dichlorodihydrofluorescein diacetate (DCHF-DA; >97%), 2′,7′-dichlorofluorescein (DCF; reagent grade) and $NaH_2PO_4 \cdot 2H_2O$ (>98%) were purchased from Sigma Aldrich, Alfa Aesar and Merck. Methanol (>99.8%) was purchased from VWR Chemicals. Ultrapure water (0.055 μS cm^{-1}, GenPure UV, Fisher Scientific GmbH) was used for sample preparation and analysis. All Stock solutions were stored in a refrigerator at 9 °C and were protected from light. DCHF-DA was stored in a refrigerator at −10 °C.

2.2 Recycling and poling procedures

In order to investigate the catalytic durability of the pyrocatalysts, the unpoled BT100 was recycled four times. The recycling was done directly after centrifugation within the previous pyrocatalytic activity experiments. The precipitated powders from several experiments were combined in a centrifugation tube (PE; 15 mL) and subsequently suspended and washed with ultrapure water. After centrifugation (3858 rcf; 10 min), the supernatant was replaced with fresh ultrapure water and this procedure was repeated eight times in order to remove all residual DCF. The washed and precipitated powder was then dried and carefully de-agglomerated by hand into a fine, homogeneous powder.

For poling, the BT samples were pressed (4.9 kN) without additives into circular discs with a diameter of 10 mm and 2 mm thickness. Then, these unsintered powder compounds

This journal is © the Owner Societies 2020

Phys. Chem. Chem. Phys., 2020, **22**, 23464–23473 | **23465**

were placed between two copper plates used as electrodes and poled under a nominal electric field of 2 kV mm^{-1} for 5 s in air. In order to be usable as suspended pyrocatalysts, the poled BT discs were carefully de-agglomerated by hand into fine, homogeneous powders.

2.3 Pyrocatalyst characterization

The crystal structures of BT samples were characterized by using X-ray diffraction (XRD, Rigaku MiniFlex600) with Cu-Kα radiation (λ = 1.54059 Å) over the range of 2θ from 20 to 90° with a scanning rate of 0.008° s^{-1}. The unit cell parameters and weight fractions were obtained via Rietveld refinement of the XRD data. The instrumental broadening and shapes of reflection profiles were calibrated and fitted with program MAUD[16] using the diffraction pattern of LaB$_6$ standard powder. Scanning electron microscopy (SEM) was used to investigate the BT powder morphology with a JSM-7001F (JEOL). The BT samples were dried, mounted on carbon pads, coated with carbon and then inserted into the microscope. At the cathode, an acceleration voltage for the electrons of 15 kV was set. Nitrogen adsorption/desorption isotherms of the BT samples were measured by physical adsorption of nitrogen (N$_2$) at about 77 K on a Quantachrome Autosorb IQ instrument. Prior to the measurements, the powders were degassed at 30 °C for 3 h under vacuum. The specific surface area S_{BET} was calculated by the Brunauer–Emmett–Teller (BET) method.

2.4 Pyrocatalytic activity experiments

To compare the ROS-induced oxidation capability of pyroelectric BT in aqueous solution, the DCF redox assay was used.[35] The DCHF-based reaction protocol was introduced by Carthcart et al. and further modified in a previous study (Scheme S1, ESI†).[36,37] This method was proven pH- and cation-independent over a wide range; it offers a high precision and enables the determination and consideration of autoxidation processes. A DCHF reaction solution was prepared by dissolving DCHF-DA in methanol (140 μL per mg DCHF-DA) and adding 0.01 M NaOH (570 μL per mg DCHF-DA) to trigger a complete deesterification of DCHF-DA to DCHF within 30 min. Finally, 25 mM NaH$_2$PO$_4$ (1.6 mL per mg DCHF-DA) was used to neutralize the base and the DCHF solution was diluted with ultrapure water to a concentration of 1 μM. In order to get reliable results, all solvents were degassed prior to use and all stock, reaction and sample solutions were protected from light and air during all procedures.

In a typical pyrocatalytic experiment, 60 mg of BT was placed within a micro tube (PP, amber, V_{max} = 1.85 mL) and suspended in 1750 μL DCHF reaction solution. The micro tube was sealed with Parafilm and shaken thoroughly. The thermal excitation of the suspended pyroelectric powders was realized with the help of a thermomixer (heating/cooling thermomixer MKR13, Hettich Benelux) equipped with an aluminum block for 24 micro tubes. Up to 12 micro tubes were placed in every second slot of the aluminum block while the remaining slots were left free (Fig. S1, ESI†). The oxidation experiments were carried out with thermal cycles between 32.5 and 69.9 °C inside the micro tubes

and simultaneous shaking at 1200 rpm. The internal temperature Θ_{in} was measured with a type K thermocouple (NiCr-Ni, ±1.5 °C) directly placed into the reaction tube. Prior to the temperature program, the reaction tubes were equilibrated for 5 min in the pre-heated aluminum block (32.5 °C). The temperature program consisted of four uniform cycles with a length of 40 min each (Fig. 1(a)) followed by a 5 min cooling phase back to 20 °C (Fig. S2, ESI†). The preset temperature Θ_P and the
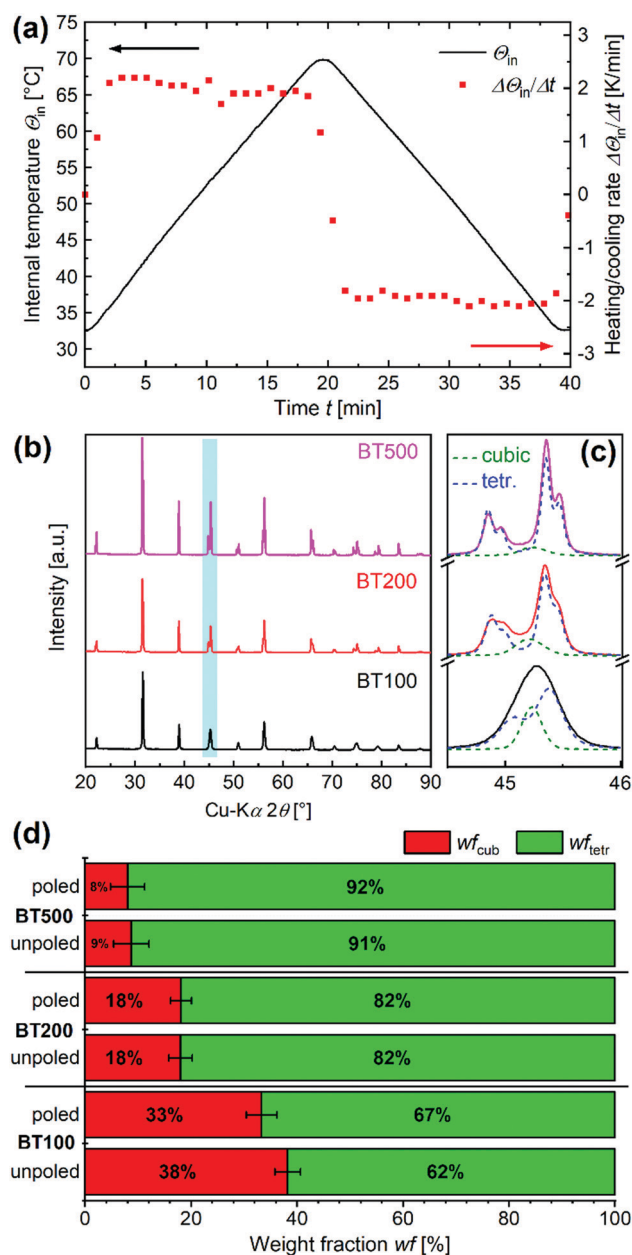

Fig. 1 (a) Measured temperature inside the reaction vessel Θ_{in} over time t and corresponding heating/cooling rate $\Delta\Theta_{in}/\Delta t$ for one thermal cycle used in the DCHF-oxidation experiments. (b) XRD patterns (c) and enlarged XRD patterns of the unpoled BaTiO$_3$ powders with nominal particle sizes of 100, 200 and 500 nm (BT100, BT200, BT500). (d) Weight fraction distribution of ferroelectric tetragonal (wf$_{tetr}$) and paraelectric cubic (wf$_{cub}$) BaTiO$_3$ phases for poled and unpoled samples.

measured temperature of the aluminum block Θ_{Al} (internal thermocouple) are displayed in Fig. S3, ESI.† The heating and cooling rates were kept constant at around +2 K min^{-1} and −2 K min^{-1} (Fig. 1(a)). The samples were then centrifuged twice at 20 °C (17 300 rcf, 5 and 15 min) to remove all BT particles. Immediately afterwards, the fluorescence intensity of the supernatant was measured. Every experiment was performed twice and the relative error of c_{DCF} corresponds to the standard deviation.

2.5 Analysis methods

Fluorescence measurements of DCF were conducted with a fluorescence detector (FP-4025, Jasco) which was equipped with a square cell holder for 10 × 10 mm square cells (Type 3/G/10, Starna Scientific). The wavelengths for excitation and emission were 480 and 525 nm and a detector gain of 1 was used. In a typical measurement 400 µL of a sample were diluted with 2900 µL degassed ultrapure water. The DCF stock solution (50 µM) was prepared by dissolving DCF in methanol (234 µL per mg DCF) and subsequent dilution of this methanolic solution with 25 mM NaH$_2$PO$_4$·2H$_2$O (2.33 mL per mg DCF). In order to get reliable results, it was crucial to protect the samples from light during the whole measurement process to prevent further DCHF oxidation. The fluorescence intensities correlated with the DCF concentration c_{DCF} in a linear fashion (Fig. S4, ESI†). The quantitative analysis was done by external calibration with standards in three concentration ranges and threefold measurements. In Table S1 (ESI†) calibration parameters for the linear regressions are displayed.

3 Results and discussion

3.1 Pyrocatalyst characterization

XRD was used to analyze the phase compositions of BT samples (unpoled powders in Fig. S5–S7, ESI†). In Fig. 1(b) and (c), the XRD patterns for the unpoled BT samples are compared in detail. For the fine-grained BT100, the peak at 2θ of 45.2° is broad, whereas it shows an increasing but not complete splitting for BT samples containing larger particles (BT200 and BT500; Fig. 1(c)). This development indicates a mixture of paraelectric cubic (COD 1507757, $Pm\bar{3}m$) and ferroelectric tetragonal phase (COD 1507756, $P4mm$) with an increasing

percentage of the latter.[38,39] Rietveld refinement method was used to further investigate the phase compositions of the BT samples. The complete results for the unpoled as well as the poled BT are listed in Tables S2 and S3 (ESI†).

In addition, the weight fractions of ferroelectric tetragonal (wf$_{tetr}$) and paraelectric cubic (wf$_{cub}$) BaTiO$_3$ phases are compared in Fig. 1(d). As indicated in the ongoing splitting of the peak at 2θ of 45.2°, wf$_{tetr}$ rises with the increasing nominal particle diameter from 61.8 ± 2.4% up to 91.3 ± 3.3% for the unpoled BT batches (Fig. 1(c)). This result can be confirmed by the results of Benke et al.[30] The refinement for BT with a size of about 150 nm resulted in a wf$_{tetr}$ of 75.4 ± 1.7%. Furthermore, Lan et al. found a wf$_{tetr}$ of about 0% for BT with a size <100 nm and wf$_{tetr}$ of about 60 and 80% for BT with sizes between 100 and 300 nm although the exact particle sizes are difficult to determine from the relevant SEM micrographs.[40] Additionally, Benke et al. found out that poling of their BT had no significant impact on the diffraction pattern and that only an insignificant amount of the cubic phase was converted to tetragonal. We can confirm these findings for BT samples with different nominal particle sizes when comparing the results for unpoled and poled BT (Tables S2, S3, ESI† and Fig. 1(d)). However, the results show that the tetragonal is the dominant phase for all BT, which means that all of them are ferroelectric and thus pyroelectric.

SEM was used to analyze the morphological and structural properties of the unpoled BT samples (Fig. 2). The particles of the powder sample with a nominal particle diameter of 100 nm (BT100) have an irregular round shape and a particle size between 100 and 200 nm (Fig. 2(a)). Powder samples of BT200 consist of particles with a size between 180 and 350 nm and show a transition from a round to an angular shape (Fig. 2(b)). For BT500, the particles show a mixture of different angular particle shapes and most particles have a size between 0.5 and 1.0 µm (Fig. 2(c)). The particles in BT100 and BT200 are agglomerated in random, micrometer-sized spheres. The poling process had no influence on the particle shape or size.

In addition to the particle size and shape, the BET specific surface area S_{BET} of all poled and unpoled powders was measured and is shown in Fig. S8 (ESI†). S_{BET} increases with decreasing particle size from 2.3 m^2 g^{-1} for BT500 up to 9.4 m^2 g^{-1} for BT100. The poling process resulted only for
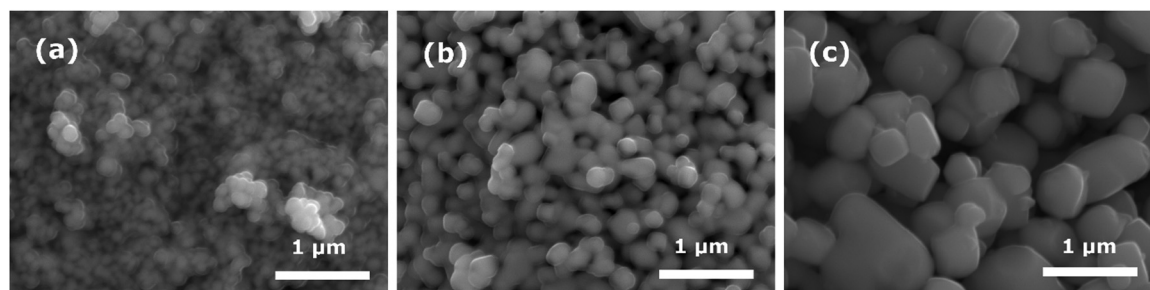

Fig. 2 SEM micrographs of unpoled BaTiO$_3$ powders with nominal particle sizes of 100, 200 and 500 nm (BT100, BT200, BT500).

This journal is © the Owner Societies 2020

Phys. Chem. Chem. Phys., 2020, 22, 23464–23473 | 23467

BT100 in a slight increase of S_{BET} (+11%), while no significant change was observed for BT200 and BT500.

3.2 Pyrocatalytic activity – BT100

The pyrocatalytic activity of BT100 nanoparticles was characterized by their ability to oxidize DCHF into DCF under a cyclic thermal excitation between 32.5 and 69.9 °C with 2 K min^{-1} (Scheme S1, ESI†). Fig. 3(a) demonstrates the increase of the characteristic fluorescence spectra of the oxidized DCF after 0 to 8 thermal cycles. Additionally, the DCF concentration c_{DCF} from experiments with an increasing number of thermal cycles was plotted in Fig. 3(b). c_{DCF} increased nearly linearly with the thermal cycle count up to 492 nM DCF for 8 cycles. This corresponds to a conversion of 49% based on the initial DCHF concentration $c_{0,DCHF}$. In a reference experiment without pyrocatalyst, less than 14 nM DCF was generated through thermal cycling alone. These findings demonstrate that the pyrocatalyst BT100 is responsible for the oxidation of DCHF into DCF under thermal cycling.

In a next step, the dependence of c_{DCF} from the powder amount β_{BT100} for the standard temperature program with four thermal cycles was determined in the range between 1.7 and 66.7 mg mL^{-1}. As shown in Fig. 3(c), there is a linear correlation between c_{DCF} and β_{BT100} over the whole range (7.7 nM DCF per mg mL^{-1} BT100). This result corresponds to results of our previous study with BT200 (1.2 nM DCF per mg mL^{-1} BT200).[37] Wu et al. and Qian et al. on the other hand found that the pyrocatalytic degradation of rhodamine B with BiFeO$_3$ and ZnO powders reached a plateau for a low β of 1 mg mL^{-1}.[41,42] For the piezocatalytic degradation of RhB and Acid Orange 7 with sonicated suspensions of K$_{0.5}$Na$_{0.5}$NbO$_3$ and Pb(Zr$_{0.52}$Ti$_{0.48}$)O$_3$, an optimum and a plateau was reached at higher β values of 4 mg mL^{-1} and 12.5 mg L^{-1}.[43,44] In these studies, the reduction or saturation of the pyro- or piezocatalytic degradation efficiencies at higher values of β were explained by the increased collision probability between suspended particles. Each collision increases the recombination probability of pyro- or piezoelectrically induced opposite surface charges, which are necessary for pollutant degradation. This explanation is comprehensible, but as can be seen from the broad range for β found in literature between 1 and 12.5 mg mL^{-1}, there have to be additional influencing factors like the material (e.g. pyro-/piezoelectric coefficient, permittivity, morphology, size), reaction (e.g. type/concentration of pollutant, pH, conductivity) and process
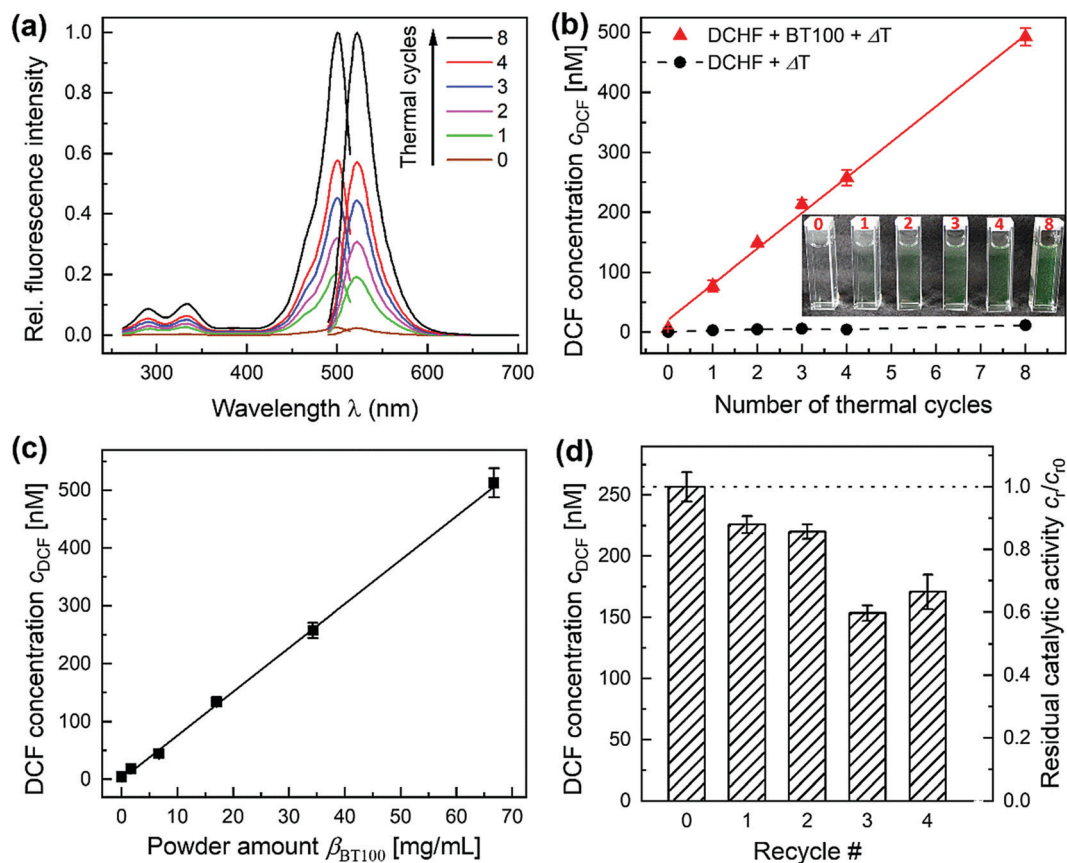

Fig. 3 Pyrocatalytic activity of the BaTiO$_3$ catalyst powder BT100 (100 nm nominal particle size) after thermal treatment: (a) fluorescence excitation and emission spectra (λ_{em} = 525 nm; λ_{ex} = 480 nm) and (b) DCF concentration c_{DCF} with ("ΔT + BT100") and without pyrocatalyst ("ΔT only") after 0 to 8 thermal cycles. Inset: Color change of the DCHF solution after 0 to 8 thermal cycles. (c) DCF concentration c_{DCF} versus powder amount β_{BT100}. (d) DCF concentration c_{DCF} and residual catalytic activity c_r/c_{r0} after recycling. DCF: 2′,7′-dichlorofluorescein; DCHF: 2′,7′-dichlorodihydrofluorescein; ΔT: thermal cycling.

23468 | Phys. Chem. Chem. Phys., 2020, **22**, 23464–23473

This journal is © the Owner Societies 2020

parameters (*e.g.* temperature, fluid mechanics). Given that many parameters in this study differ greatly from previous studies, a much wider linear range for the linear correlation between c_{DCF} and β_{BT100} is plausible.

Next, the stability and reusability of BT100 was investigated. As shown in Fig. 3(d), the residual catalytic activity c_r/c_{r0} decreases discontinuously. After twofold recycling, the amount of oxidized DCHF decreased only slightly (87.5%) and dropped down to 68 ± 6% after four recycling steps. XRD measurements revealed no notable changes in crystal structure and phase composition. In addition, S_{BET} decreased only slightly by less than −5%. A possible explanation for the decrease of pyro-catalytic activity can be a consecutive adsorption of DCHF and DCF on active sites of the BaTiO$_3$ particles in combination with a slight aggregation of smaller particles. As the reusability of powder catalysts is crucial for a future application, strategies for preserving the residual catalytic activity after several recy-cling steps should be developed. Possible approaches are the washing of the catalyst with organic solvents or the disaggrega-tion of particles with the help of ultrasound.

3.3 Pyrocatalytic activity – size dependency

After studying the correlation between c_{DCF} and β_{BT100} as well as the catalyst reusability, experiments with BT of different nom-inal particle diameters d_{nom} of 100, 200 and 500 nm (BT100, BT200, BT500) were performed. Fig. 4(a) shows that c_{DCF} is decreasing with increasing d_{nom} of unpoled BT. In order to reveal how much of the increased reactivity of the fine-grained BT100 can be explained by its larger surface area, c_{DCF} was plotted as a function of S_{BET} (Fig. 4(b)). Although the number of data points is small, c_{DCF} is found to be proportional to S_{BET} in good approximation. Accordingly, the increased reactivity of the fine-grained BT100 in this study can be mainly be explained by its larger surface area.

Nevertheless, the authors would like to point out that for BT containing smaller particles, further parameters exist which can outweigh the influence of S_{BET} (Table 1). For instance, in a direct comparison Wu *et al.* found that a BT with low particle sizes and a XRD pattern with cubic symmetry features tetra-gonality had a lower pyrocatalytic performance for RhB degra-dation than a BT with larger particles and a XRD pattern showing tetragonal symmetry features.[29] These findings are supported by another study of Wu *et al.* regarding the role of the ferroelectric polarization on the piezocatalytic activity of annealed BT.[34] They determined the highest piezocatalytic performance for RhB degradation for an annealed BT with medium particle size, tetragonality c/a and S_{BET}. The perfor-mance of annealed BT containing smaller and larger particles declined (Table 1).

An explanatory approach, which combines and mostly explains the previously mentioned results, is that the size-dependency of the pyrocatalytic activity has its origin in a combination of opposing, size-dependent changes in S_{BET} and the crystallographic composition. As S_{BET} increases with a decreasing particle size ($S_{BET} \sim 1/d$), wf_{tetr} and c/a are decreasing (Fig. S8, ESI† and Fig. 1(d), Table S2, ESI†).[45,46]
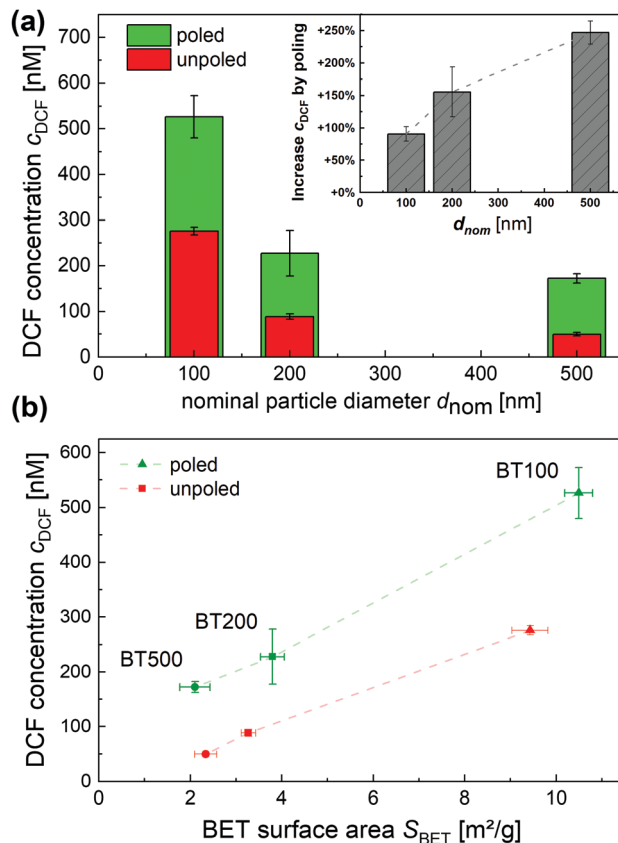

Fig. 4 Pyrocatalytic activity of poled and unpoled BaTiO$_3$ catalysts with nominal particle sizes of 100, 200 and 500 nm (BT100, BT200, BT500). (a) 2′,7′-Dichlorofluorescein (DCF) concentration c_{DCF} after thermal treat-ment. Inset plot: Relative increase of c_{DCF} through poling of BT. (b) Plot of c_{DCF} as a function of BET surface area S_{BET}. BET: Brunauer–Emmett–Teller.

While S_{BET} correlates to the adsorption capability, wf_{tetr} defines the fraction of BT that is actually pyroelectric, *i.e.* catalytically active, and ($c/a - 1$) correlates with the pyroelectric coefficient and how much charge is generated during temperature changes. A hypothetical progression of the size-dependent pyrocatalytic activity $c_{DCF} = f(d_{nom})$ of unpoled BT was derived from the assumption that the pyrocatalytic activity is in a rough estimation proportional to the product of S_{BET}, wf_{tetr} and ($c/a - 1$) and is shown in Fig. 5. Based on this schematic plot, BT pyrocatalysts can be categorized into three classes depending on their particle size. BT catalysts with large particle sizes (>1 μm) belong to the first class C-I and should have a low pyrocatalytic activity as a consequence of a very low S_{BET} (≪1 m^2 g^{-1}). BT catalysts with particle sizes between 1 μm and 100 nm belong to the second class C-II. In this class, S_{BET} increases drastically with decreasing particle size, outweighing the moderate decline of wf_{tetr} and ($c/a - 1$). As a result, c_{DCF} increases drastically when the particle size is decreased and S_{BET} is increased, as shown in this study for BT100, BT200 and BT500 (Fig. 4(b)). The third class C-III covers BT catalysts with further decreased particle sizes down to around 30 nm. The ferroelectric, tetragonal phase is suppressed due to bound-ary effects below this critical particle size d_{crit} (C-0).[47] In this

Table 1 Comparison of material parameters with the pyro- or piezocatalytic performance of differently sized BaTiO$_3$ powders

Particle size	Tetragonal phase weight fraction wf$_{tetr}$	BET specific surface area S_{BET}	Catalytic activity	Ref(s).
100–200 nm (BT100)	62%	9.4 m^2 g^{-1}	Increase c_{DCF} (pyro): 276 nM	
180–350 nm (BT200)	82%	3.3 m^2 g^{-1}	89 nM	This work
0.5–1.0 μm (BT500)	91%	2.3 m^2 g^{-1}	50 nM	
≤100 nm[a]	Low[a]	—[b]	Degradation degree RhB (pyro): 26%[a]	Wu et al.[29]
150–300 nm[a]	High[a]	—[b]	48%[a]	
<100 nm[a]	Low[a]; $c/a = 1.001$[a]	21.1 m^2 g^{-1}	Rate constant MO degradation (piezo): 0.014 min^{-1}[a]	
100–350 nm[a]	Medium[a]; $c/a = 1.005$[a]	4.7 m^2 g^{-1}	0.019 min^{-1}	Wu et al.[34]
≫1 μm[a]	High (100%[a]); $c/a > 1.011$	0.23 m^2 g^{-1}	0.005 min^{-1}	

[a] Estimate based on the experimental data reported. [b] Not applicable; wf$_{tetr}$: tetragonal phase weight fraction; S_{BET}: Brunauer–Emmett–Teller (BET) specific surface area; BTX00: BaTiO$_3$ powder with X00 nm nominal particle size; c_{DCF}: concentration of 2′,7′-dichlorofluorescein (DCF); RhB: rhodamine B; MO: methyl orange.

third class, wf$_{tetr}$ and (c/a − 1) drop down to zero, whereas S_{BET} only triples with decreasing particle size. These opposing tendencies lead to a weakening of the increase of c_{DCF} until a maximum in pyrocatalytic activity is reached at the optimal particle size. Below this optimal particle size, the decrease of wf$_{tetr}$ and (c/a − 1) outweighs the increase of S_{BET}, causing c_{DCF} to drop down rapidly towards zero at d_{crit}. It should be noted, however, that the exact development of the catalytic activity as a function of particle size as well as the optimal particle size depend on additional factors such as the excitation mechanism, the model reaction or the particle shape. Nevertheless, the results of both studies of Wu et al. are in good agreement with this classification.[29,34] The BT compared in the studies of Wu et al. (Table 1) belong to different classes. In both studies, the fine-grained BT belongs to the third and the medium-sized BT to the second class. Considering that the catalytic activity for BT catalysts of the third class is sensitive to slight changes of wf$_{tetr}$ and (c/a − 1), the lower piezocatalytic activity of the fine-grained BT compared to the medium-sized BT despite its much higher S_{BET} is plausible. Further studies should be performed

to confirm this explanatory approach in order to be able to predict optimal particle sizes for piezo- and pyrocatalysts.

3.4 Pyrocatalytic activity – poling effect

A strong increase of the catalytic activity of pyrocatalysts has been achieved by implementing a poling treatment. The influence of this on the pyrocatalytic activity of BT batches with increasing particle size was investigated and is shown in Fig. 4(a). Poling led to a strong and size-dependent increase of c_{DCF} whereby the strongest relative increase of +247% was found for BT500 with the largest particle. For the finest powder, BT100, the increase turned out to be only +91%. Changes in the particle shape/size, S_{BET} or wf$_{tetr}$ cannot explain these results, as they were not significantly affected by the poling. The literature does not describe changes in these parameters for poled BT either.[30,31,34] A summary of relevant parameters and results of previous studies on the influence of poling on the piezo- and pyrocatalytic activity of BT is given in Table 2 for comparison. These studies are difficult to compare as different excitation mechanisms (thermal vs. mechanical), poling procedures and model reactions were used. In addition, the available material characterization data differ. However, the combination with the fully comparable data of this study results in a largely consistent picture: (i) poling of BT with a particle size larger than ca. 200 nm (BT200, BT500; Chen et al.) up to several micrometers (Wu et al.) and with a high wf$_{tetr}$ leads to strong improvements of piezo- and pyrocatalytic activity.[31,34] (ii) For fine-grained BT with a considerably reduced wf$_{tetr}$ of ≪80% and a particle size near 100 nm, only marginal (Benke et al.) or reduced (BT100) positive effects can be achieved by poling.[30]

A possible explanation for similar observations in piezocatalysis was provided by Wu et al. and links the ferroelectric polarization of individual BaTiO$_3$ particles with their size, crystal and domain structure (schematically shown in Fig. 6).[34] Small BaTiO$_3$ particles below the critical size d_{crit} of about 30 nm have a cubic phase and are therefore paraelectric and non-pyroelectric (Fig. 6(a1) and (b1)). Particles with a higher particle size up to about 100 nm are ferroelectric single
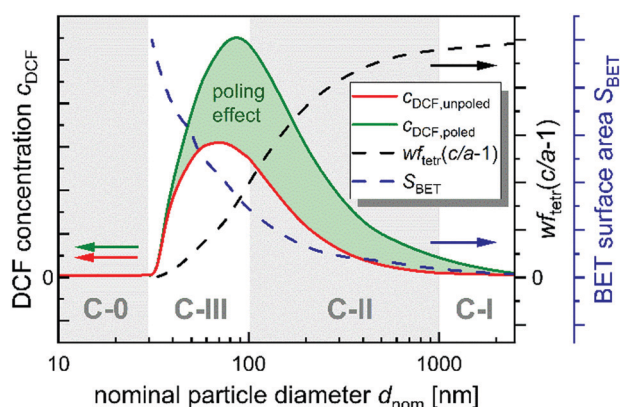

Fig. 5 Hypothetical progression of c_{DCF}, the product of the tetragonal phase weight fraction wf$_{tetr}$ times the tetragonality (c/a − 1) and S_{BET} as a function of the nominal particle diameter d_{nom}. BET: Brunauer–Emmett–Teller.

Table 2 Comparison of material and poling parameters with the effect of poling on the pyro- or piezocatalytic performance of $BaTiO_3$ powders

Particle size	Tetragonal phase weight fraction wf_{tetr}	BET specific surface area S_{BET}	Poling parameters	Poling effect on catalytic activity	Ref(s).
100–200 nm (BT100)	$61.8 \pm 2.4\%$ (unpol.) $66.7 \pm 2.9\%$ (poled)	$9.4\ m^2\ g^{-1}$ (unpol.) $10.5\ m^2\ g^{-1}$ (poled)		Increase c_{DCF} (pyro): $+91\%$	
180–350 nm (BT200)	$82.0 \pm 2.2\%$ (unpol.) $81.9 \pm 2.0\%$ (poled)	$3.3\ m^2\ g^{-1}$ (unpol.) $3.8\ m^2\ g^{-1}$ (poled)	$2\ kV\ mm^{-1}$; 5 s; powder pellet	$+155\%$	This work
0.5–1.0 μm (BT500)	$91.3 \pm 3.3\%$ (unpol.) $92.0 \pm 3.2\%$ (poled)	$2.3\ m^2\ g^{-1}$ (unpol.) $2.1\ m^2\ g^{-1}$ (poled)		$+247\%$	
ca. 150 nm	75.4%	—[b]	$3\ kV\ mm^{-1}$; 1 h; powder pellet	Coumarin dosimetry (pyro): Marginal effect	Benke et al.[30]
ca. 350 nm	Tetragonal phase	—[b]	$1.5/3/5\ kV\ mm^{-1}$; 30 min; 110 °C; Au-coated wafer	Decomposition ratio RhB (pyro): $+100/300/560\%$	Chen et al.[31]
$\gg 1$ μm[a]	100%[a] $c/a > 1011$[a]	$0.23\ m^2\ g^{-1}$	$2/4\ kV\ mm^{-1}$; 30 min; powder pellet	Rate constant MO degradation (piezo): $+35$[a]$/80\%$	Wu et al.[34]

[a] Estimate based on the experimental data reported. [b] Not applicable; wf_{tetr}: tetragonal phase weight fraction; S_{BET}: Brunauer–Emmett–Teller (BET) specific surface area; BTX00: $BaTiO_3$ powder with X00 nm nominal particle size; RT: room temperature; c_{DCF}: concentration of 2′,7′-dichlorofluorescein (DCF); RhB: rhodamine B; MO: methyl orange.
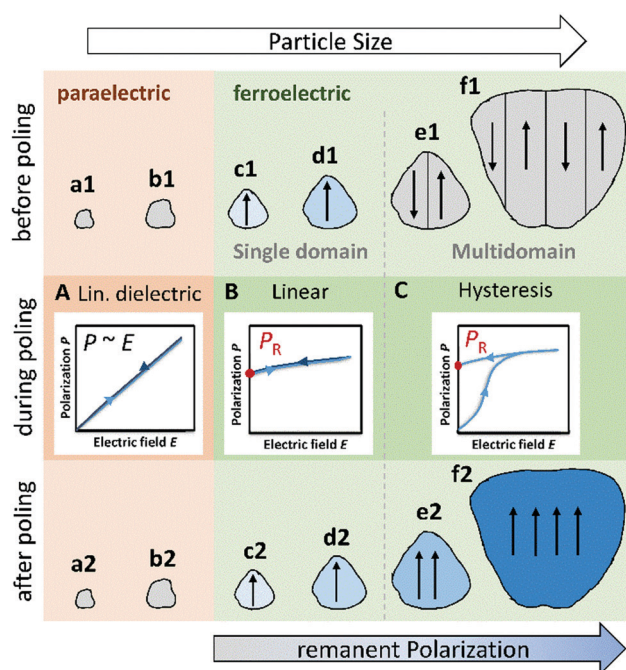

Fig. 6 Schematic representation of the relationships between particle size, polarization, crystal and domain structure (a1)–(f1) before poling and (a2)–(f2) after poling with a sufficiently strong external electric field. Typical progressions of polarization *versus* electric field (P–E) for (A) paraelectric, (B) ferroelectric single-domain, and (C) ferroelectric multidomain crystals (demonstration only; not to scale).

crystals with a single ferroelectric domain (Fig. 6(c1) and (d1)) Larger particles develop a multidomain structure with a domain size of tens to hundreds of nanometers depending on the particle size (Fig. 6(e1) and (f1)). With continuous growth, for example during an annealing procedure, $BaTiO_3$ particles can additionally develop a polycrystalline structure through partial sintering.[47–49] In their virgin state, individual

domains in a multidomain single crystal as well as individual crystallites in a polycrystalline particle should be randomly oriented, resulting in a macroscopic polarization of zero.[50] Since a reduction in polarization has a negative effect on the pyroelectric coefficient and thus on the pyrocatalytic activity, coarse-grained $BaTiO_3$ pyrocatalysts can benefit from poling.[34,51] During the poling procedure, the ferroelectric domains in individual polycrystalline particles and in multidomain single crystals align along the direction of a sufficiently strong electric field (Fig. 6(e2) and (f2)). This alignment results in an increased remanent polarization P_R of these particles after the field is reduced back to zero (ferroelectric hysteresis; Fig. 6(C)).[52] The increase of P_R is beneficial for the pyroelectric coefficient and thus increases the pyrocatalytic activity of these particles.[34,51] On the contrary, the pyrocatalytic activity of small ferroelectric particles with only a single domain should be independent of the poling treatment (Fig. 6(c2) and (d2)). For these particles, the polarization rises and falls linearly with the external electric field, so that there should be no further significant increase in P_R (Fig. 6(B)).[53] Consequently, the positive effect of poling reduces with decreasing particle size. The further the particle size distribution of a $BaTiO_3$ powder is shifted towards smaller particle sizes, the higher the proportion of paraelectric and single-domain ferroelectric $BaTiO_3$ particles that do not benefit from poling.

Considering all previously discussed findings, theoretical explanations and comparisons with literature, a hypothetical progression of the size-dependent pyrocatalytic activity $c_{DCF} = f(d_{nom})$ for poled BT was derived based on assumptions explained in Section 3.3 (Fig. 5). Additionally, the influence of the size-dependent crystal and domain structure on the poling behavior and the resulting increase in pyrocatalytic activity was estimated. While the relative positive effect on pyrocatalytic activity should increase with increasing d_{nom}, the absolute effect should have an optimum for medium-sized BT. Again, it should be noted that the exact development of the catalytic activity as a function of particle size for poled BT depend on

This journal is © the Owner Societies 2020

Phys. Chem. Chem. Phys., 2020, **22**, 23464–23473 | **23471**

additional factors such as the excitation mechanism, the model reaction or the particle shape. Therefore, further studies should be performed to confirm this explanatory approach in order to be able to predict optimal particle sizes for poled piezo- and pyrocatalysts.

However, considering all previously discussed findings, a basic future strategy for maximizing the pyrocatalytic performance of BaTiO$_3$ nanoparticles for DCHF oxidation can be developed: (I) S_{BET} should be maximized through a further decrease of the particle size while maintaining sufficiently high values for wf$_{tetr}$ and c/a. (II) All ferroelectric BT catalysts should be poled in order to increase the alignment of the intrinsic ferroelectric dipoles of multidomain or polycrystalline BaTiO$_3$ particles.

4 Conclusions

In conclusion, the interdependence between the particle size, the poling procedure and the pyrocatalytic activity of BaTiO$_3$ powders with nominal particle sizes of 100, 200 and 500 nm was revealed by using the DCF redox assay under directly comparable conditions. Based on our results, we were able to estimate and confirm the basic progression of the pyrocatalytic activity of unpoled BaTiO$_3$ powders as a function of nominal particle size. Moreover, we demonstrated that poling of pyrocatalysts leads to a strong size-dependent increase of pyrocatalytic activity. This poling effect increased with particle size up to +247% and was explained with size-dependent changes in phase composition and domain structure. Based on the findings of the experimental investigations, a future strategy for maximizing the catalytic performance of BaTiO$_3$ pyrocatalysts was developed. Further research topics are the long term and cycling stability of poled BT, the influence of poling conditions on the pyrocatalytic activity and the influence of heating/cooling rates as well as temperature range. With the help of highly active pyrocatalysts, the pyrocatalytic process can take the next step in its development into a new AOP technique for water remediation, accompanied with a great potential for thermal energy harvesting. We believe that this study provides a deeper understanding of the influence of important material parameters on the catalytic performance of pyrocatalysts.

Conflicts of interest

There are no conflicts to declare.

Acknowledgements

References

1 T. P. Van Boeckel, S. Gandra, A. Ashok, Q. Caudron, B. T. Grenfell, S. A. Levin and R. Laxminarayan, *Lancet Infect. Dis.*, 2014, **14**, 742–750, DOI: 10.1016/s1473-3099(14)70780-7.

2 K. Kummerer, *J. Environ. Manage.*, 2009, **90**, 2354–2366, DOI: 10.1016/j.jenvman.2009.01.023.

3 L. M. Bexfield, P. L. Toccalino, K. Belitz, W. T. Foreman and E. T. Furlong, *Environ. Sci. Technol.*, 2019, **53**, 2950–2960, DOI: 10.1021/acs.est.8b05592.

4 T. aus der Beek, F. A. Weber, A. Bergmann, S. Hickmann, I. Ebert, A. Hein and A. Kuster, *Environ. Toxicol. Chem.*, 2016, **35**, 823–835, DOI: 10.1002/etc.3339.

5 S. Fekadu, E. Alemayehu, R. Dewil and B. Van der Bruggen, *Sci. Total Environ.*, 2019, **654**, 324–337, DOI: 10.1016/j.scitotenv.2018.11.072.

6 P. Sehonova, Z. Svobodova, P. Dolezelova, P. Vosmerova and C. Faggio, *Sci. Total Environ*, 2018, **631–632**, 789–794, DOI: 10.1016/j.scitotenv.2018.03.076.

7 P. Falas, A. Wick, S. Castronovo, J. Habermacher, T. A. Ternes and A. Joss, *Water Res.*, 2016, **95**, 240–249, DOI: 10.1016/j.watres.2016.03.009.

8 D. Kanakaraju, B. D. Glass and M. Oelgemoller, *J. Environ. Manage.*, 2018, **219**, 189–207, DOI: 10.1016/j.jenvman.2018.04.103.

9 G. V. Buxton, C. L. Greenstock, W. P. Helman and A. B. Ross, *J. Phys. Chem. Ref. Data*, 1988, **17**, 513–886, DOI: 10.1063/1.555805.

10 D. B. Miklos, C. Remy, M. Jekel, K. G. Linden, J. E. Drewes and U. Hubner, *Water Res.*, 2018, **139**, 118–131, DOI: 10.1016/j.watres.2018.03.042.

11 S. Yan, A. Jia, S. Merel, S. A. Snyder, K. E. O'Shea, D. D. Dionysiou and W. Song, *Environ. Sci. Technol.*, 2016, **50**, 1437–1446, DOI: 10.1021/acs.est.5b04540.

12 Y. Yin, L. Shi, W. Li, X. Li, H. Wu, Z. Ao, W. Tian, S. Liu, S. Wang and H. Sun, *Environ. Sci. Technol.*, 2019, **53**, 11391–11400, DOI: 10.1021/acs.est.9b03342.

13 Y. Z. Ren, M. Franke, F. Anschuetz, B. Ondruschka, A. Ignaszak and P. Braeutigam, *Ultrason. Sonochem.*, 2014, **21**, 2020–2025, DOI: 10.1016/j.ultsonch.2014.03.028.

14 M. Dietrich, M. Franke, M. Stelter and P. Braeutigam, *Ultrason. Sonochem.*, 2017, **39**, 741–749, DOI: 10.1016/j.ultsonch.2017.05.038.

15 N. Singh and B. R. Goldsmith, *ACS Catal.*, 2020, **10**, 3365–3371, DOI: 10.1021/acscatal.9b04167.

16 M. Abinaya, R. Rajakumaran, S.-M. Chen, R. Karthik and V. Muthuraj, *ACS Appl. Mater. Interfaces*, 2019, **11**, 38321–38335.

17 C. Xu, P. Ravi Anusuyadevi, C. Aymonier, R. Luque and S. Marre, *Chem. Soc. Rev.*, 2019, **48**, 3868–3902.

18 J. You, Y. Guo, R. Guo and X. Liu, *Chem. Eng. J.*, 2019, **373**, 624–641.

19 R. Katal, M. Salehi, M. H. Davood Abadi Farahani, S. Masudy-Panah, S. L. Ong and J. Hu, *ACS Appl. Mater. Interfaces*, 2018, **10**, 35316–35326.

20 E. Gutmann, A. Benke, K. Gerth, H. Bottcher, E. Mehner, C. Klein, U. Krause-Buchholz, U. Bergmann, W. Pompe and D. C. Meyer, *J. Phys. Chem. C*, 2012, **116**, 5383–5393.

21 C. Forman, I. K. Muritala, R. Pardemann and B. Meyer, *Renewable Sustainable Energy Rev.*, 2016, **57**, 1568–1579.

22 J. Ma, L. Chen, Z. Wu, J. Chen, Y. Jia and Y. Hu, *Ceram. Int.*, 2019, **45**, 11934–11938.

23472 | *Phys. Chem. Chem. Phys.*, 2020, **22**, 23464–23473

This journal is © the Owner Societies 2020

23 M. Sharma, V. P. Singh, S. Kumar and R. Vaish, *J. Appl. Phys.*, 2020, **127**, 135103.

24 X. Xu, L. Xiao, Y. Jia, Z. Wu, F. Wang, Y. Wang, N. O. Haugen and H. Huang, *Energy Environ. Sci.*, 2018, **11**, 2198–2207.

25 J. Schlechtweg, S. Raufeisen, M. Stelter and P. Braeutigam, *Phys. Chem. Chem. Phys.*, 2019, **21**, 23009–23016, DOI: 10.1039/c9cp02510c.

26 M. U. de Vivanco, M. Zschornak, H. Stocker, S. Jachalke, E. Mehner, T. Leisegang and D. C. Meyer, *Phys. Chem. Chem. Phys.*, 2020, **22**, 17781–17790, DOI: 10.1039/d0cp01288b.

27 S. Li, Z. Zhao, J. Zhao, Z. Zhang, X. Li and J. Zhang, *ACS Appl. Nano Mater.*, 2020, **3**, 1063–1079.

28 Y. Zhang, P. Phuong, E. Roake, H. Khanbareh, Y. Wang, S. Dunn and C. Bowen, *Joule*, 2020, **4**, 301–309, DOI: 10.1016/j.joule.2019.12.019.

29 J. Wu, N. Qin, B. Yuan, E. Lin and D. Bao, *ACS Appl. Mater. Interfaces*, 2018, **10**, 37963–37973.

30 A. Benke, E. Mehner, M. Rosenkranz, E. Dmitrieva, T. Leisegang, H. Stocker, W. Pompe and D. C. Meyer, *J. Phys. Chem. C*, 2015, **119**, 18278–18286.

31 L. Chen, H. Li, Z. Wu, L. Feng, S. Yu, H. Zhang, J. Gao, Y.-W. Mai and Y. Jia, *Ceram. Int.*, 2020, **46**, 16763–16769.

32 S. Kumar, M. Sharma, S. Powar, E. N. Kabachkov and R. Vaish, *J. Eur. Ceram. Soc.*, 2019, **39**, 2915–2922.

33 B. W. Yuan, J. Wu, N. Qin, E. Z. Lin, Z. H. Kang and D. H. Bao, *Appl. Mater. Today*, 2019, **17**, 183–192.

34 J. Wu, Q. Xu, E. Lin, B. Yuan, N. Qin, S. K. Thatikonda and D. Bao, *ACS Appl. Mater. Interfaces*, 2018, **10**, 17842–17849.

35 B. Kalyanaraman, V. Darley-Usmar, K. J. A. Davies, P. A. Dennery, H. J. Forman, M. B. Grisham, G. E. Mann, K. Moore, L. J. Roberts and H. Ischiropoulos, *Free Radical Biol. Med.*, 2012, **52**, 1–6.

36 R. Cathcart, E. Schwiers and B. N. Ames, *Anal. Biochem.*, 1983, **134**, 111–116.

37 S. Raufeisen, M. Stelter and P. Braeutigam, *PLoS One*, 2020, **15**, e0228644, DOI: 10.1371/journal.pone.0228644.

38 E. K. Al-Shakarchi and N. B. Mahmood, *J. Mod. Phys.*, 2011, **2**, 1420–1428.

39 S. Grazulis, D. Chateigner, R. T. Downs, A. F. T. Yokochi, M. Quiros, L. Lutterotti, E. Manakova, J. Butkus, P. Moeck and A. Le Bail, *J. Appl. Crystallogr.*, 2009, **42**, 726–729.

40 S. Lan, J. Feng, Y. Xiong, S. Tian, S. Liu and L. Kong, *Environ. Sci. Technol.*, 2017, **51**, 6560–6569.

41 J. Wu, W. Mao, Z. Wu, X. Xu, H. You, A. Xue and Y. Jia, *Nanoscale*, 2016, **8**, 7343–7350.

42 W. Q. Qian, Z. Wu, Y. M. Jia, Y. T. Hong, X. L. Xu, H. L. You, Y. Q. Zheng and Y. T. Xia, *Electrochem. Commun.*, 2017, **81**, 124–127.

43 A. Zhang, Z. Y. Liu, X. H. Geng, W. F. Song, J. S. Lu, B. Xie, S. M. Ke and L. L. Shu, *Ceram. Int.*, 2019, **45**, 22486–22492.

44 H. Lin, Z. Wu, Y. M. Jia, W. J. Li, R. K. Zheng and H. S. Luo, *Appl. Phys. Lett.*, 2014, **104**, 162907.

45 M. Yashima, T. Hoshina, D. Ishimura, S. Kobayashi, W. Nakamura, T. Tsurumi and S. Wada, *J. Appl. Phys.*, 2005, **98**, 014313.

46 E. Ciftci, M. N. Rahaman and M. Shumsky, *J. Mater. Sci.*, 2001, **36**, 4875–4882.

47 C. Fang, L. Y. Chen and D. X. Zhou, *Phys. B*, 2013, **409**, 83–86.

48 Y. Huan, X. H. Wang, J. Fang and L. T. Li, *J. Am. Ceram. Soc.*, 2013, **96**, 3369–3371.

49 H. I. Hsiang and F. S. Yen, *J. Am. Ceram. Soc.*, 1996, **79**, 1053–1060.

50 M. Acosta, N. Novak, V. Rojas, S. Patel, R. Vaish, J. Koruza, G. A. Rossetti and J. Rodel, *Appl. Phys. Rev.*, 2017, **4**, 041305.

51 S. B. Lang and D. K. Das-Gupta, in *Handbook of Advanced Electronic and Photonic Materials and Devices*, ed. H. Singh Nalwa, Academic Press, Burlington, 2001, pp. 1–55.

52 R. W. Whatmore, in *Springer Handbook of Electronic and Photonic Materials*, ed. S. O. Kasap and P. Capper, Springer International Publishing AG, Switzerland, 2nd edn, 2017, ch. 26, pp. 589–614.

53 S. Patel, A. Chauhan and R. Vaish, *Ferroelectrics*, 2015, **486**, 114–125.

This journal is © the Owner Societies 2020

Phys. Chem. Chem. Phys., 2020, **22**, 23464–23473 | **23473**